Showcasing research from the Group of Prof. Ling Jiang at Dalian Institute of Chemical Physics, Chinese Academy of Sciences, China

Infrared photodissociation spectroscopy of cold cationic trimethylamine complexes

Cryogenic ion-trap infrared photodissociation spectroscopy combined with a dielectric barrier discharge source was constructed to establish the general trends in the stepwise growth motif of trimethylamine $(TMA)_n^+$ complexes. The results showed a strong preference for the formation of a stable charge-shared N···N type $(TMA)_2^+$ ion core rather than a proton-transferred C···HN type ion core, evidencing that the source condition has a remarkable effect on the kinetic stability of isomers. Starting at n = 9, the additional TMA molecules form a second solvation shell, and cluster spectra show similarities to the solution phase spectrum of aqueous TMA.

As featured in:

See Ling Jiang *et al.*, *Phys. Chem. Chem. Phys.*, 2018, **20**, 25583.

ROYAL SOCIETY OF CHEMISTRY

rsc.li/pccp

Registered charity number: 207890

PCCP

PAPER

View Article Online
View Journal | View Issue

Cite this: *Phys. Chem. Chem. Phys.*, 2018, **20**, 25583

Infrared photodissociation spectroscopy of cold cationic trimethylamine complexes†

Xin Lei,[ab] Xiangtao Kong,[a] Zhi Zhao,[a] Bingbing Zhang,[ab] Dongxu Dai,[a] Xueming Yang [a] and Ling Jiang *[a]

Received 11th June 2018,
Accepted 4th July 2018

DOI: 10.1039/c8cp03672a

rsc.li/pccp

Cryogenic ion-trap infrared photodissociation spectroscopy combined with a dielectric barrier discharge source was constructed to establish the general trends in the stepwise growth motif of trimethylamine $(TMA)_n^+$ complexes. The results showed a strong preference for the formation of a stable charge-shared N···N type $(TMA)_2^+$ ion core over the proton-transferred C···HN type ion core, evidencing that the source condition has a remarkable effect on the kinetic stability of isomers. A maximum of four TMA molecules are located perpendicularly to the N···N axis of the charge-shared $(TMA)_2^+$ ion core. In the n = 7 and 8 clusters, the subsequent two TMA molecules are located at each end of the N···N axis of the $(TMA)_2^+$ ion core, completing the first coordination shell. Starting at n = 9, the additional TMA molecules form a second solvation shell, and the cluster spectra show similarities to the solution phase spectrum of aqueous TMA.

1. Introduction

Trimethylamine (TMA) is a molecule with one of the largest proton affinities (~949 kJ mol^{-1})[1] and often participates in the formation of strong hydrogen-bond networks.[2–4] The TMA molecule contains two nonequivalent types of hydrogen atoms (H_a and H_b; Scheme 1). The C–H_b bond is antiperiplanar to the nitrogen lone pair, with its bond length 0.0126 Å longer than that of the C–H_a bond.[5] The polarizabilities and dipole derivatives of the C–H_a and C–H_b bonds are also different.[6] A number of fundamental questions on TMA clusters are thus to be addressed: (1) what factor is essential for the stepwise growth motif; (2) what is the relative kinetic stability of the charge-shared N···N type and proton-transferred C···HN type structures; (3) what is the preference between the N···H_a and N···H_b intermolecular interactions, *etc.* These issues are crucial for the molecular-level understanding of various chemical, geophysical, and atmospheric processes.

Mass spectrometry and optical spectroscopy of gas-phase clusters provide detailed energetic and structural information that is difficult to extract from bulk measurements.[7–13] Measurements on isolated cluster ions are particularly attractive due to their size-selectivity and signal sensitivity. Even though the solvation environment in the microsolvated cluster ions is not identical to that in a solution, *e.g.* there are typically no counter ions, the underlying intermolecular interaction is the same and can be studied by adding one molecule at a time, providing ample testing grounds for theoretical modeling.[7–13] A pioneering infrared photodissociation (IRPD) spectroscopic study of the cationic TMA dimer, $(TMA)_2^+$, demonstrated the coexistence of the charge-shared N···N type and proton-transferred C···HN type structures.[14] Interestingly, results on the proton-transferred C···HN type structure showed that the methyl groups of cationic trimethylamine are highly acidic, revealing the characteristic properties of radical cations with alkyl groups. IRPD spectroscopy of the binary $H^+(TMA)_nH_2O$ (n = 1–22) clusters indicated that the proton localizes on the TMA moiety regardless of cluster size.[15,16] A matrix-isolation IR study of TMA/H_2O clusters exhibited that the cluster is formed in the vapor phase (as opposed to being a result of the diffusion of the trapped species) and is related to its large stabilization energy because of strong cooperative effects in its hydrogen-bond system.[17] In the TMA/H_2SO_4/H_2O clusters, the complex formed between TMA and H_2SO_4 is of ionic character due to proton transfer of the H^+ proton from H_2SO_4 to TMA to form a new N–H bond and the replacement of the intramolecular

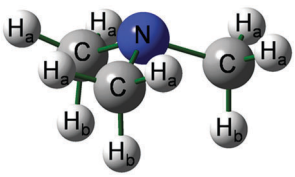

Scheme 1 The structure of TMA with labeling.

[a] *State Key Laboratory of Molecular Reaction Dynamics, Dalian Institute of Chemical Physics, Chinese Academy of Sciences, 457 Zhongshan Road, Dalian 116023, China. E-mail: ljiang@dicp.ac.cn*
[b] *University of Chinese Academy of Sciences, 19A Yuquan Road, Beijing 100049, China*

† Electronic supplementary information (ESI) available. See DOI: 10.1039/c8cp03672a

O–H bond in H_2SO_4 by a strong intermolecular N–H···O hydrogen bond.[18]

Herein, we report gas-phase infrared spectra of the $(TMA)_n^+$ (n = 3–9) clusters. The $(TMA)_n^+$ cations were generated by the soft ionization of pulsed supersonic beams *via* a dielectric barrier discharge (DBD) source[19] and characterized using mass-selected IRPD spectroscopy combined with cryogenic ion trap technology. The structural assignment of the IRPD spectra was aided by quantum chemical calculations. The combination of experimental and calculated IR spectra allows for an identification of the general trends in the stepwise growth motif of the $(TMA)_n^+$ complexes.

2. Experimental details

The experimental apparatus is schematically depicted in Fig. 1. The apparatus included four major sections: DBD source, quadrupole mass spectrometer, cryogenic ion trap, and time-of-flight (TOF) mass spectrometer. The supersonic beam of TMA complexes was produced from the expansion using an Even-Lavie valve (1). The DBD source (2) was mounted on a 0.125 mm nozzle of the Even-Lavie valve. The excitation source was based on a dielectric barrier discharge in the pulsed supersonic beam. It produced cold beams of both positively and negatively charged cluster ions with high efficiency and stability. These ions moved with low velocity and high Mach number.

The cluster ions were passed through a 4 mm diameter skimmer (Beam Dynamics, Model 50.8) (3). The mass spectrum of the clusters ions was measured by a quadrupole mass spectrometer (4) equipped with a Conversion Dynode Electron Multiplier (6). The cluster ion of interest was selected by the quadrupole mass filter, deflected by 90° in an electrostatic quadrupole deflector (5), and focused by a set of Einzel lens (7) into a gas-filled 3D Paul trap (Jordan TOF Products, Inc.) (8). The mass resolution of the quadrupole mass filter was set to be sufficiently high ($\Delta m/Z \leq \sim 1$) to prevent contamination by other cluster species. The 3D Paul trap was encased in an oxygen-free high-purity copper block that was in good thermal contact with the cold head (second stage) of a two-stage closed-cycle helium refrigerator (Sumitomo SRDK-415E-F50H; 1.5 W cooling power at 4.2 K) (9). The ion trap was enclosed in an aluminum cylinder for thermal shielding, which was connected to the first stage of the helium refrigerator operated at 50 K. To allow continuous ion accumulation and ion thermalization, the ion trap was continuously filled with helium buffer gas at an ion-trap temperature of 15 K. After loading the trap for 98 ms, all ions were extracted from the trap and focused by a set of Einzel lens (10) and deflecting plates (11) both temporally and spatially into the center of the extraction region of an orthogonally mounted linear TOF mass spectrometer (12).[20–22] Here, the ion packet was irradiated with a tunable IR laser. After IR laser irradiation, the fragment and parent ions were accelerated and mass analyzed using the TOF mass spectrometer (13–15). The output signals from the chevron configured microchannel plates (15) were amplified by a preamplifier (SRS, Model SR445A, 350 MHz), digitized by a two-channel 200 MHz–1 GHz/8 bit DAQ (FCFR-USB9982B), and transferred into a computer. IR spectra were recorded by monitoring all ion intensities simultaneously as a function of the dissociation IR laser wavelength and were normalized by the IR power. Typical spectra were obtained by scanning the dissociation laser in steps of 2 cm^{-1} and averaging over 600 laser shots at each wavelength.

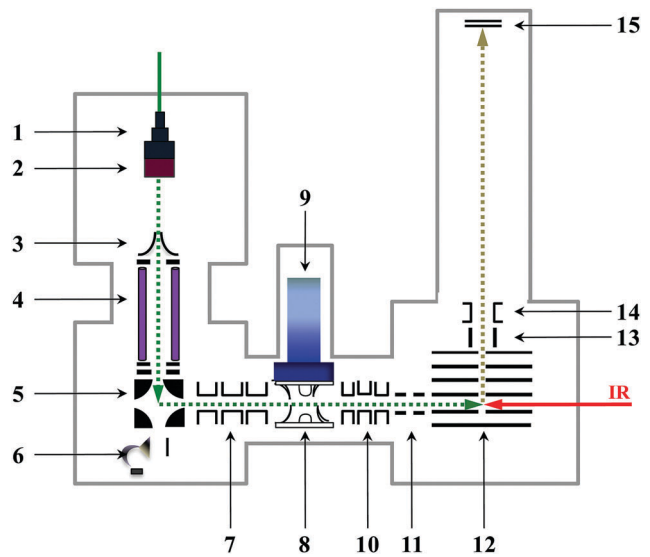

Fig. 1 Schematic of the experimental IRPD setup used in the present study (see the text for details): (1) Even-Lavie valve; (2) DBD; (3) skimmer; (4) quadrupole mass spectrometer; (5) electrostatic quadrupole deflector; (6) conversion dynode electron multiplier; (7 and 10) Einzel lens; (8) 3D Paul trap; (9) cold head of a two-stage closed cycle helium refrigerator; (11) deflecting plate; (12) modified Wiley–McLaren extraction stack, (13) focusing lens; (14) ion deflectors; and (15) microchannel plate detector.

The tunable IR laser beam was generated by a KTP/KTA optical parametric oscillator/amplifier system (OPO/OPA, Laser-Vision) pumped by an injection-seeded Nd:YAG laser (Continuum Surelite EX). The system provided tunable IR output radiation from 700 to 7000 cm^{-1} with a 7 ns pulse width. The linewidth of the mid-IR output was $\sim$1 cm^{-1}. The wavelength of the OPO laser output was calibrated using a laser spectrum analyzer (HighFinesse, OSA).

3. Computational methods

Quantum chemical calculations were carried out using the Gaussian 09 package.[23] The M062X method with the 6-311+G(d,p) basis set was employed. The integral grid used for the M062X calculations was a pruned (99 590) grid (the "ultrafine" grid as defined by Gaussian 09). The relative energies, binding energies, dissociation energies, and energy barriers were calculated at 0 K with zero-point vibrational energies. A scaled factor of 0.944 was taken from the Database of Frequency Scale Factors for Electronic Model Chemistries maintained by D. G. Truhlar *et al.* (https://comp.chem.umn.edu/freqscale/version3b2.htm) and used for the harmonic vibrational frequencies,[24] in order to account for anharmonicities and for method-dependent systematic errors

on the calculated harmonic force constants. The resulting stick spectra were convoluted by a Gaussian line shape function with a width of 6 cm^{-1} (FWHM).

4. Results and analysis

A typical quadrupole mass spectrum of cluster ions produced by the DBD source is shown in Fig. 2. The unprotonated $(TMA)_n^+$ and protonated $H^+(TMA)_x$ clusters can be observed. Additional signals of the $[N(CH_3)_2(TMA)_m]^+$ species can also be observed with relatively weak intensities as compared to $(TMA)_n^+$. The TOF mass spectrometer was used to confirm the mass distribution of the size-selected clusters. For instance, the TOF mass spectra of quadrupole-mass-selected $(TMA)_5^+$ and $H^+(TMA)_5^+$ (Fig. 3a) indicate that the unprotonated $(TMA)_n^+$ cluster can be differentiated from the protonated $H^+(TMA)_x$ cluster. When the unprotonated $(TMA)_n^+$ cluster was selected for the IRPD measurement (*vide infra*), a trace of the protonated $H^+(TMA)_x$ cluster was present (Fig. 3b), evidencing the negligible contribution of the protonated clusters.

The experimental IRPD spectra of $(TMA)_n^+$ (n = 3–9) clusters are shown in Fig. 4. Band positions are summarized in Table 1. Seven bands, labeled A–G, are observed in the C–H stretching region (2700–3100 cm^{-1}). Band A is centered at 2988 cm^{-1} in the n = 3 cluster, which red-shifts slightly to 2982 cm^{-1} at n = 9. Similarly, bands B–G show small red-shifts by 4–15 cm^{-1}. The experimental and theoretical results for each individual cluster are presented in the following sections. Optimized structures of $(TMA)_n^+$ (n = 3–6) are illustrated in Fig. 5. For each cluster up to n = 9, the comparison of the experimental IRPD spectrum to the simulated IR spectra is shown in Fig. 6–10, respectively.

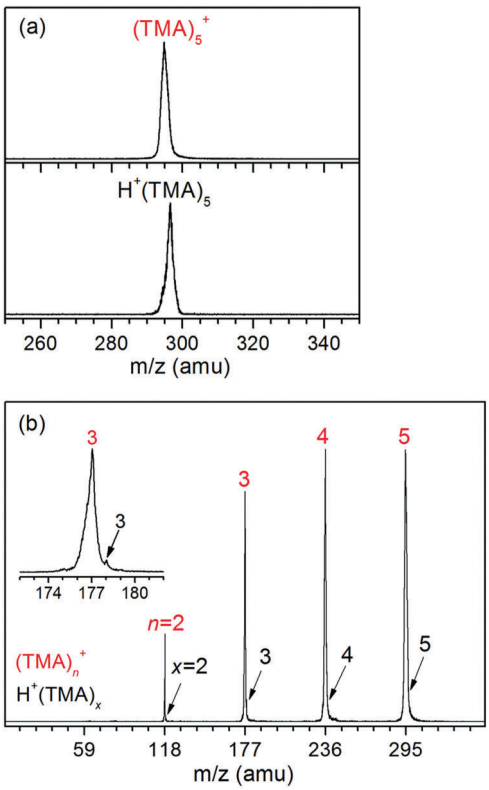

Fig. 3 TOF mass spectra of quadrupole-mass-selected $(TMA)_5^+$ and $H^+(TMA)_5^+$ when IR laser is off (a) and IR photodissociation for $(TMA)_5^+$ when IR laser is on (b). The mass spectrum in the 172–182 amu region is enlarged in the inset.

$(TMA)_3^+$

In the lowest energy isomer of $(TMA)_3^+$, labeled as 3-I, the two TMA molecules form a N···N type $(TMA)_2^+$ ion core, in which the positive charge is intermolecularly delocalized over the dimer through the interaction between the nonbonding orbitals of the nitrogen atoms (Fig. 5). The third TMA molecule is located perpendicularly to the N···N axis of the ion core and the N atom of the third TMA molecule interacts with the adjacent three H_a atoms of the ion core. The 3-II isomer lies 2.18 kJ mol^{-1} higher than 3-I, in which the third TMA molecule is located

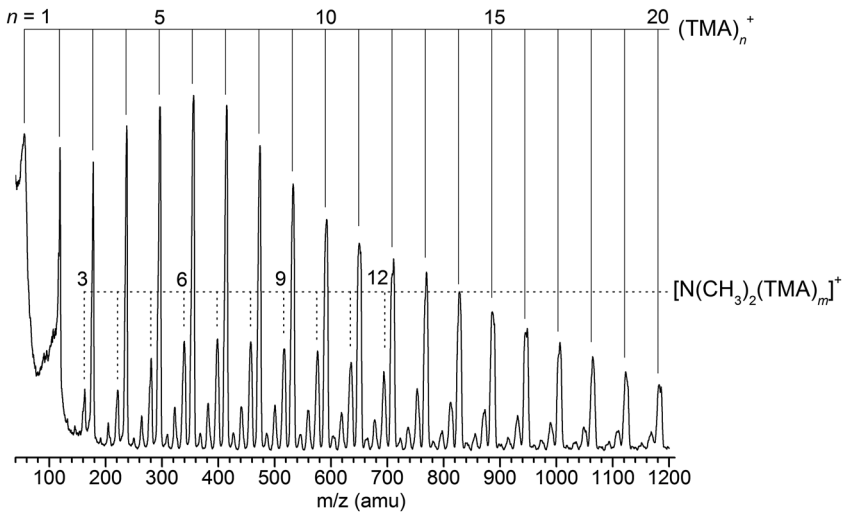

Fig. 2 Quadrupole mass spectrum of the cationic clusters produced by the DBD source using a gas mixture of 2.5% TMA seeded in 3.5 MPa helium carrier gas.

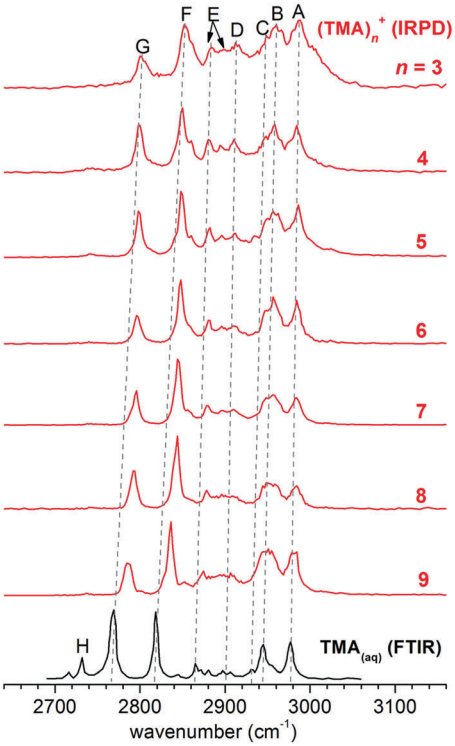

Fig. 4 Experimental IRPD spectra of $(TMA)_n^+$ ions with n = 3–9. The FTIR spectrum of TMA in liquid Kr is shown at the bottom.[34]

along the N···N axis of the N···N type $(TMA)_2^+$ ion core and its N atom interacts with the adjacent three H_b atoms of the ion core. The 3-III isomer has a C···HN type $(TMA)_2^+$ ion core, in which a proton of a methyl group in the ionized moiety is intermolecularly transferred to the nitrogen atom of the neutral moiety and is shared between the carbon and nitrogen atoms. Isomer 3-III lies 7.89 kJ mol^{-1} above isomer 3-I.

In the calculated IR spectrum of 3-I (Fig. 6), the 2992 cm^{-1} band (labeled a) is due to the CH_{2a} asymmetric stretching of the $(TMA)_2^+$ core ($\nu_{A(core\text{-}CH_{2a})}$), which well reproduces the experimental band A (2988 cm^{-1}). The calculated band b at 2956 cm^{-1} is attributed to the CH_{2a} asymmetric stretching of neutral TMA ($\nu_{A(neu\text{-}CH_{2a})}$), which is consistent with the experimental value of band B (2960 cm^{-1}). The CH_3 asymmetric stretching of the $(TMA)_2^+$ core ($\nu_{A(core\text{-}CH_3)}$) is predicted at 2942 cm^{-1} (band c), which is in agreement with the experimental value of band C (2948 cm^{-1}). The CH_3 asymmetric stretching of neutral TMA ($\nu_{A(neu\text{-}CH_3)}$) is predicted at 2918 cm^{-1} (band d), and it is observed experimentally at 2912 cm^{-1} (band D). The calculated band e at 2865 cm^{-1} is assigned to the CH_3 symmetric stretching of the $(TMA)_2^+$ core ($\nu_{S(core\text{-}CH_3)}$), which reproduces the experimental band E (2884 cm^{-1}). The calculated band f at 2835 cm^{-1} is due to the CH_3 symmetric stretching of neutral TMA ($\nu_{S(neu\text{-}CH_3)}$), which is consistent with the experimental band F (2852 cm^{-1}). Note that the IR intensities of the calculated bands are different from the observed ones (Fig. 6). As listed in Table 2, the spectra for the n = 3 cluster might be measured in the multiphoton absorption regime, and the relative intensities of the bands in the experimental IR spectra may differ significantly from those in the linear absorption spectra.[9] IR laser power dependence tests were carried out to avoid saturation effects (not shown here). The simulated IR spectrum of 3-II is very similar to that of 3-I. The main difference of the simulated IR spectrum of 3-III compared to 3-I and 3-II is that an intense band is calculated at 2400 cm^{-1}, which is due to the vibration of the shared proton, but it is not seen in the experimental spectrum.

In summary, the calculated IR spectra of isomers 3-I and 3-II are in reasonable agreement with the experiment, except that band G (2800 cm^{-1}) is not reproduced theoretically. The coexistence of isomers 3-I and 3-II is likely here. The presence of isomer 3-III can be ruled out on the basis of the absence of the vibration of the shared proton in the experimental spectrum. The extra band G could be due to the Fermi resonance behavior of the light isotopologue; these are often close in energy and can strongly mix through cubic terms in the potential function.[15–17,25] In the C–H Fermi resonances in the formate ion reported recently,[25] the dominant interactions occur between the C–H stretching fundamental and both the in-plane and out-of-plane bending overtones. An intense band of the Fermi-mixing type was observed at 2820 cm^{-1} in the $H^+(TMA)H_2O$ cluster.[17] Recent *ab initio* anharmonic calculations of neutral monomethylamine clusters $(MMA)_n$ (n = 2–4) indicated that the FR stemmed from the coupling between the stretching and bending overtones of the CH_3 group.[26] Multidimensional anharmonic calculations for the monomethylamine, dimethylamine, and trimethylamine clusters are in progress. The effects of the methyl group and cluster size on the Fermi resonance in the monomethylamine, dimethylamine, and trimethylamine clusters will be systematically discussed in a separate paper.

Table 1 Peak positions (in cm^{-1}) in the experimental IRPD spectra of $(TMA)_n^+$

Label	n = 3	n = 4	n = 5	n = 6	n = 7	n = 8	n = 9	TMA$_{(aq)}$[a]	Assignment
A	2988	2986	2986	2984	2984	2984	2982	2976	CH_{2a} asymmetric stretching of the $(TMA)_2^+$ core ($\nu_{A(core\text{-}CH_{2a})}$)
B	2960	2958	2956	2956	2956	2948	2950	2944	CH_{2a} asymmetric stretching of neutral TMA ($\nu_{A(neu\text{-}CH_{2a})}$)
C	2948	2948	2948	2947	2947	2945	2944	2931	CH_3 asymmetric stretching of $(TMA)_2^+$ core ($\nu_{A(core\text{-}CH_3)}$)
D	2912	2912	2912	2910	2910	2908	2907	2901	CH_3 asymmetric stretching of neutral TMA ($\nu_{A(neu\text{-}CH_3)}$)
E	2898	2896	2896	2896	2896	2896	2894	2880	CH_3 symmetric stretching of the $(TMA)_2^+$ core ($\nu_{S(core\text{-}CH_3)}$)
	2884	2882	2882	2881	2879	2878	2875	2864	
F	2852	2850	2848	2848	2844	2844	2837	2818	CH_3 symmetric stretching of neutral TMA ($\nu_{S(neu\text{-}CH_3)}$)
G	2800	2798	2798	2796	2796	2793	2786	2769	Fermi resonance
H	—	—	—	—	—	—	—	2730	Overtone of C–H stretching

[a] The FTIR spectrum of TMA in liquid Kr is shown as TMA$_{(aq)}$.[34]

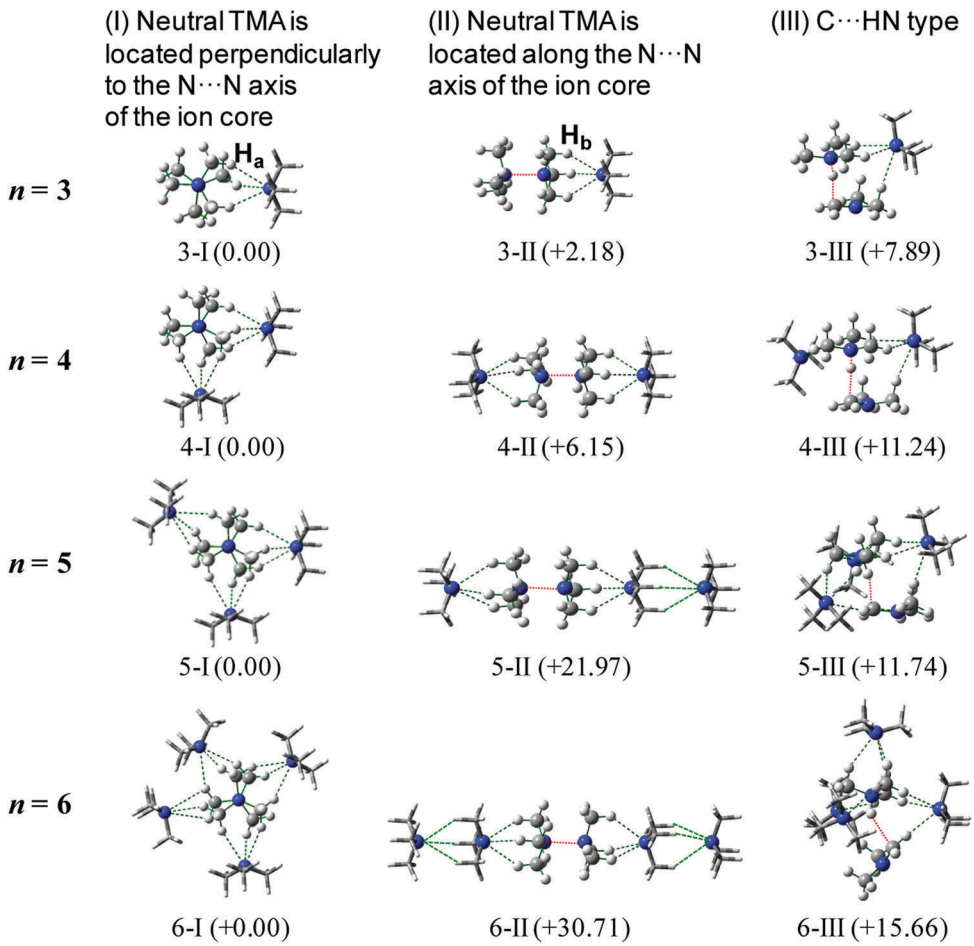

Fig. 5 Optimized structures of $(TMA)_n^+$ (n = 3–6). Relative energies are given in kJ mol^{-1}. The $(TMA)_2^+$ ion core is shown as the ball and bond type and the neutral TMA is depicted as the tube type.

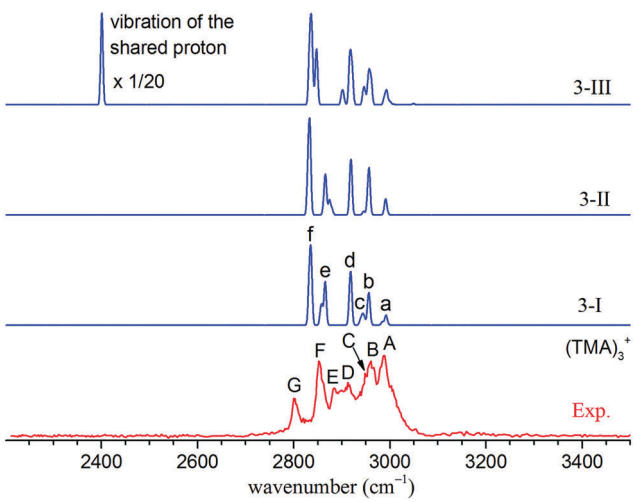

Fig. 6 Comparison of the experimental IRPD spectrum of $(TMA)_3^+$ (bottom panel) with the simulated IR spectra of the three conformers (upper panels).

$(TMA)_4^+$

The lowest energy isomer (4-I) consists of a N···N type $(TMA)_2^+$ ion core (Fig. 5). The N atom of the fourth TMA molecule interacts with the adjacent three H_a atoms of the ion core. The 4-II isomer lies 6.15 kJ mol^{-1} higher than isomer 4-I. In isomer 4-II, the neutral TMA molecules are added to the two opposite sides of the $(TMA)_2^+$ ion core along to the N···N axis. The third isomer, 4-III, lies 11.24 kJ mol^{-1} above 4-I and contains a C···HN type proton-transferred structure, which is similar to the 3-III structure. The simulated IR spectra of 4-I and 4-II are similar and reproduce the experimental bands A–F (Fig. 7). In the simulated spectrum of 4-III, the vibration of the shared proton is predicted at 2587 cm^{-1}, which is not observed experimentally.

Table 2 M062X/6-311+G(d,p) lowest dissociation energies (E_{diss}, kJ mol^{-1}) for the dissociation of one TMA molecule from the most stable structure of $(TMA)_n^+$ (n = 3–9) and the number of IR photons required to overcome the dissociation limit

$(TMA)_n^+$	E_{diss}	Number of IR photons required to overcome the dissociation limit at 3000 cm^{-1}
n = 3	42.15	2
n = 4	40.51	2
n = 5	37.65	2
n = 6	30.48	1
n = 7	31.95	1
n = 8	25.73	1
n = 9	27.73	1

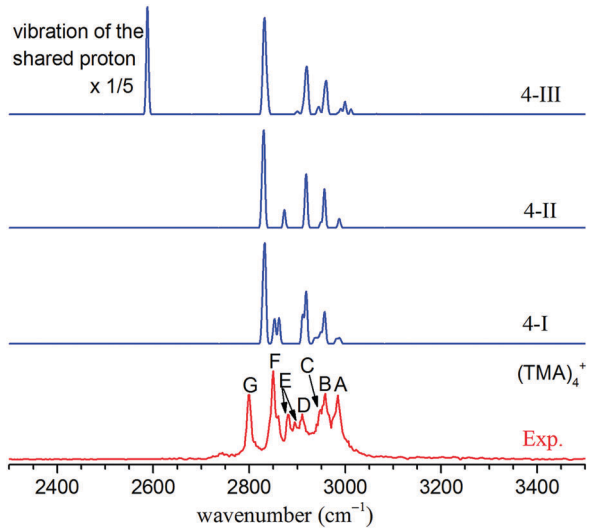

Fig. 7 Comparison of the experimental IRPD spectrum of $(TMA)_4^+$ (bottom panel) with the simulated IR spectra of the three conformers (upper panels).

It thus appears that isomer 4-III does not contribute to the experimental spectrum.

$(TMA)_5^+$

The lowest energy isomer for $(TMA)_5^+$, 5-I, could be viewed as the derivative of 4-I, in which the fifth TMA molecule forms three N···H_a intermolecular interactions with the ion core, as shown in Fig. 5. The 5-II isomer is built upon adding the fifth TMA molecule along the N···N axis, in which the N atom of the fifth TMA interacts with the adjacent three H_b atoms of one neutral TMA. Isomer 5-II lies 21.97 kJ mol^{-1} higher than isomer 5-I. The 5-III isomer consists of a C···HN type structure and lies 11.74 kJ mol^{-1} above 5-I. The simulated IR spectrum of 5-I agrees best with experiment (Fig. 8). In the simulated IR spectrum of 5-II, band F is split into two distinct features, which is not observed experimentally. In 5-III, a strong C···H hydrogen bond is calculated at 2700 cm^{-1}, which is absent from the experimental spectrum.

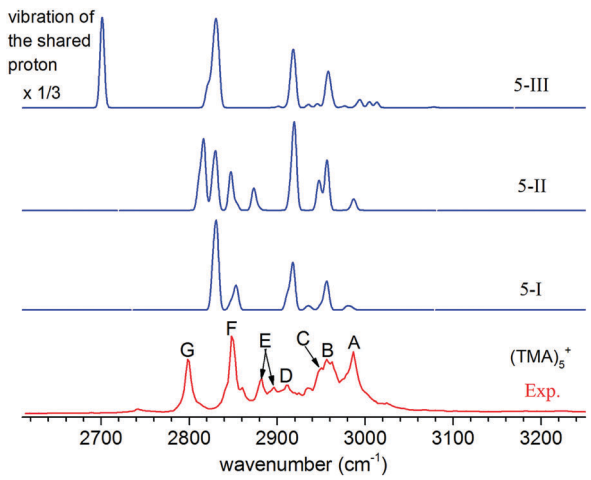

Fig. 8 Comparison of the experimental IRPD spectrum of $(TMA)_5^+$ (bottom panel) with the simulated IR spectra of the three conformers (upper panels).

$(TMA)_6^+$

The lowest energy isomer (6-I) is based on 5-I and the sixth TMA fills the remaining three H_a atoms of the ion core (Fig. 5). In the 6-II isomer, the sixth TMA is located along the N···N axis, which lies 30.71 kJ mol^{-1} higher than isomer 6-I. The 6-III isomer has a C···HN type proton-transferred structure, which lies 15.66 kJ mol^{-1} above 6-I. The simulated IR spectrum of 6-I is in accordance with experiment (Fig. 9). The energetically higher-lying isomer 6-II could not be readily formed under the present experimental conditions, and its calculated IR spectrum could not fit as well with the experiment as compared to that of 6-I. In the simulated IR spectrum of 6-III, the N–H stretching and C–H asymmetric stretching vibrations of the proton-transferred H^+(TMA) unit are calculated at 3010 and 2996 cm^{-1}, respectively, which are absent from the experimental spectrum.

$(TMA)_n^+$ (n = 7–9)

It can be inferred from the above analysis that the n-II and n-III isomers (n = 5 and 6) are not responsible for the experimental spectra. Then, the n-II and n-III structures are not considered in the n = 7–9 clusters. In the calculated lowest energy structure of $(TMA)_7^+$ (7-I) (Fig. 10), the seventh TMA molecule is located along the N···N axis of the ion core with the formation of three N···H_b intermolecular interactions. In the lowest energy isomer for $(TMA)_8^+$ (8-I), the eighth TMA molecule fills the remaining three H_b atoms of the ion core, completing the first coordination shell. In the 9-I isomer, the ninth TMA extends the TMA–TMA network *via* the N···H intermolecular interactions and forms a second solvation layer. The simulated IR spectra of the 7-I, 8-I, and 9-I isomers are consistent with experiment (Fig. 10).

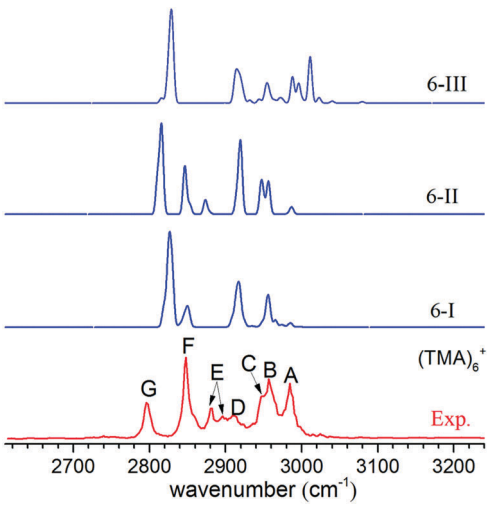

Fig. 9 Comparison of the experimental IRPD spectrum of $(TMA)_6^+$ (bottom panel) with the simulated IR spectra of the three conformers (upper panels).

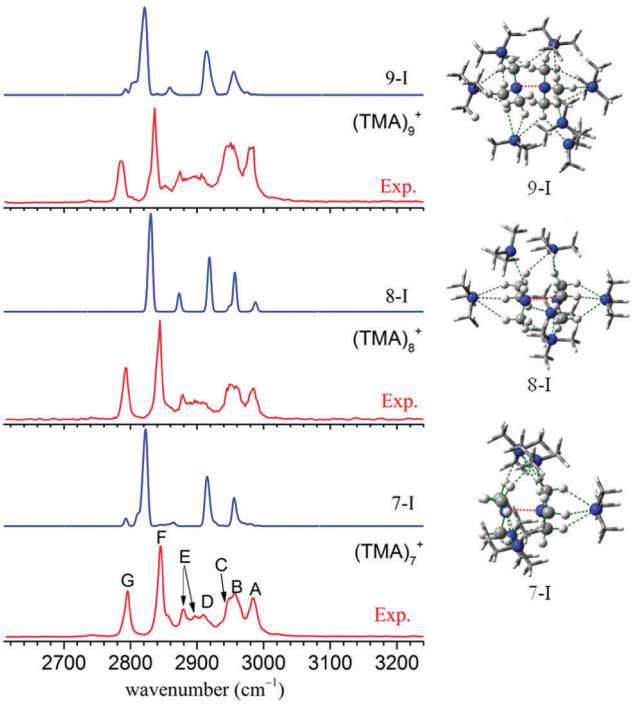

Fig. 10 Comparison of the experimental IRPD spectra of $(TMA)_n^+$ (n = 7–9) with the simulated IR spectra of the most-likely conformers.

5. Discussion

The overall agreement between the experimental and theoretical results allows the general trends in the stepsize solvation motifs of the $(TMA)_n^+$ complexes to be established. The presence of a stable charge-shared $(TMA)_2^+$ ion core in the n = 3–9 clusters was identified by infrared spectroscopy and quantum chemical calculations. The higher lying structure of the C···HN proton-transferred ion core type was not observed under the present experimental conditions. The neutral TMA molecule is located perpendicularly to the N···N axis of the charge-shared $(TMA)_2^+$ ion core and preferentially forms three N···H_a intermolecular interactions. A maximum of four TMA molecules interact directly with these H_a sites of the charge-shared $(TMA)_2^+$ ion core. In the n = 7 and 8 clusters, the subsequent two TMA molecules are located at each end of the N···N axis of the $(TMA)_2^+$ ion core and form the N···H_b intermolecular interactions, completing the first coordination shell. Starting at n = 9, additional TMA molecules are found to form a second solvation shell. It can be seen from Table S1 (ESI†) that the N···N bond length of the $(TMA)_2^+$ core in the $(TMA)_n^+$ (n = 3–9) ions decreases from 2.337 Å at n = 3 to 2.312 Å at n = 9, indicating that the N···N bond strength recovers gradually with the increase of cluster size. Similar evidence could be obtained from the Wiberg bond order of N···N bond of the $(TMA)_2^+$ core (Table S1, ESI†).

The N···H_a–C and N···H_b–C angles in the 3-I and 3-II isomers (Fig. 5) were calculated to be ~154° and ~138° at the M062X/6-311+G(d,p) level of theory, respectively. Consequently, the N···H_a–C angle is much closer to the ideal collinear alignment than the N···H_b–C angle, implying that the formation of the N···H_a intermolecular interaction is more favorable than that of the N···H_b intermolecular interaction. The N···H_a and N···H_b distances in the 3-I and 3-II isomers were calculated to be ~2.47 and ~2.54 Å, respectively, which also supports the preference of the N···H_a intermolecular interaction superior to the N···H_b intermolecular interaction.

Previous IRPD spectroscopy of $(TMA)_2^+$ exhibited the coexistence of both the charge-shared structure and the proton-transferred structure, where the $(TMA)_2^+$ cation was generated by the 118 nm VUV photoionization of the neutral dimer in supersonic expansion and the fragment ions originating from the vibrational predissociation were detected using the quadrupole mass spectrometer without a cold ion trap.[14] In contrast, the $(TMA)_n^+$ clusters were created from a DBD prior to the nozzle expansion under the present experimental conditions, which offers the following benefits of the DBD source:[19] (1) the discharge is initiated in the filaments that rapidly charge the dielectric in nanoseconds, which prevents hot spots from forming; (2) the uniform coverage of the barrier electrode prevents the avalanche process that produces arcing in the gas; (3) the electron- and ion-energy distribution in such a DBD source is low (1–10 eV). Consequently, the cold ion beams could be efficiently formed. For $(TMA)_3^+$, the equilibrium constant in between the charge-shared (isomer 3-I) and proton-transferred (isomer 3-III) structures is predicted to be 25 at 298 K and 15 098 at 100 K at the M062X/6-311+G(d,p) level of theory, respectively, indicating that the temperature has a significant effect on the kinetic stability of isomers 3-I and 3-III. Below 100 K, the kinetic stability of isomer 3-I is overwhelmingly superior to that of isomer 3-III. Note that the barrier for the isomerization from 3-III to 3-I is calculated to be 25.76 kJ mol^{-1} at the M062X/6-311+G(d,p) level of theory. Such an isomerization barrier could be small so that the population of isomer 3-I is dominant in the equilibrium of isomers 3-I and 3-III at low temperatures. Thus, the absence of the higher lying structure of the proton-transferred structure in the $(TMA)_n^+$ clusters implies that the temperature of the ionic beam in the DBD source is lower than that of the 118 nm VUV photoionization.

Analogously, previous experimental studies on the $(CS_2)_2^-$ anions have also shown that the isomer population depends on the source conditions.[27–33] The weakly-bound $CS_2{\cdot}CS_2^-$ ion–molecule complex is mainly produced in the supersonic expansion.[33] Thermal heating affords sufficient energy to overcome the isomerization barriers and shifts the isomer population *via* a weakly bound isomer, in which the electron is delocalized over the complete complex, to lower-energy covalently bound structures.

It can be seen from Fig. 4 that the frequencies of bands A–G monotonically shift toward their aqueous values as the number of TMA molecules is increased. For the n = 9 cluster, all the absorption bands are within 19 cm^{-1} of their positions in aqueous solution (Table 1) and the gas-phase cluster spectra show similarities to the solution-phase spectrum, indicating that the first solvation shell is nearing completion. In the condensed phase spectrum, band H was assigned to the overtone of C–H stretching,[34] which is not observed in the present

cluster spectra. As demonstrated before for the first overtone of the antisymmetric O–H stretching in the IRMPD spectra of $[MgNO_3(H_2O)_n]^+$ (n = 1–3),[35] the intensity of a higher order excitation is more sensitive to the IR laser power. Recently, infrared-vacuum ultraviolet spectroscopy of the neutral monomethylamine dimer also indicated that an overtone or combination band disappears at low IR laser power.[36] The absence of band H in the IR spectra of the $(TMA)_n^+$ clusters indicates that the present infrared spectra were measured in the scheme of linear photodissociation cross section.

6. Conclusion

In this work, a dielectric barrier discharge source was used to generate cold trimethylamine cluster cations. Gas-phase infrared photodissociation spectra of cryogenically-cooled $(TMA)_n^+$ (n = 3–9) were measured in the 2200–3500 cm^{-1} spectral range. The combination of experimental and simulated IR spectra allows for an identification of the general trends in the stepsize formation of coordination shells of the $(TMA)_n^+$ complexes. The formation of a stable charge-shared N···N type $(TMA)_2^+$ ion core is preferred, whereas a higher lying structure of the proton-transferred C···HN type ion core is absent under the present experimental conditions. A maximum of four TMA molecules interact directly with these H_a sites of the charge-shared $(TMA)_2^+$ ion core. For n = 7 and 8, the subsequent two TMA molecules form the N···H_b intermolecular interactions, completing the first coordination shell. Starting at n = 9, additional TMA molecules are found to form a second solvation shell. Similarities and differences of the cluster spectra with the infrared spectrum of aqueous TMA have been discussed in light of these trends.

Conflicts of interest

There are no conflicts to declare.

Acknowledgements

This work was supported by the National Natural Science Foundation of China (Grants 21673231 and 21688102) and the Strategic Priority Research Program of the Chinese Academy of Sciences (Grant XDB17000000). L. J. acknowledges the Hundred Talents Program of Chinese Academy of Sciences. We greatly appreciate advice from Professor Knut R. Asmis and Dr Xuebin Wang on the design of experimental apparatus.

References

1 E. P. L. Hunter and S. G. Lias, *J. Phys. Chem. Ref. Data*, 1998, **27**, 413–656.
2 R. Zhang, A. Khalizov, L. Wang, M. Hu and W. Xu, *Chem. Rev.*, 2012, **112**, 1957–2011.
3 C. Qiu and R. Zhang, *Phys. Chem. Chem. Phys.*, 2013, **15**, 5738–5752.
4 M. Kulmala, J. Kontkanen, H. Junninen, K. Lehtipalo, H. E. Manninen, T. Nieminen, T. Petaja, M. Sipila, S. Schobesberger, P. Rantala, A. Franchin, T. Jokinen, E. Jarvinen, M. Aijala, J. Kangasluoma, J. Hakala, P. P. Aalto, P. Paasonen, J. Mikkila, J. Vanhanen, J. Aalto, H. Hakola, U. Makkonen, T. Ruuskanen, R. L. Mauldin, III, J. Duplissy, H. Vehkamaki, J. Back, A. Kortelainen, I. Riipinen, T. Kurten, M. V. Johnston, J. N. Smith, M. Ehn, T. F. Mentel, K. E. J. Lehtinen, A. Laaksonen, V.-M. Kerminen and D. R. Worsnop, *Science*, 2013, **339**, 943–946.
5 W. F. Murphy, F. Zerbetto, J. L. Duncan and D. C. McKean, *J. Phys. Chem.*, 1993, **97**, 581–595.
6 W. F. Murphy, D. C. McKean, A. M. Coats, A. Kindness and N. Wilkie, *J. Raman Spectrosc.*, 1995, **26**, 763–770.
7 X.-B. Wang, *J. Phys. Chem. A*, 2017, **121**, 1389–1401.
8 O. Dopfer and M. Fujii, *Chem. Rev.*, 2016, **116**, 5432–5463.
9 N. Heine and K. R. Asmis, *Int. Rev. Phys. Chem.*, 2015, **34**, 1–34.
10 A. B. Wolk, C. M. Leavitt, E. Garand and M. A. Johnson, *Acc. Chem. Res.*, 2014, **47**, 202–210.
11 A. Fujii and K. Mizuse, *Int. Rev. Phys. Chem.*, 2013, **32**, 266–307.
12 F. N. Keutsch, J. D. Cruzan and R. J. Saykally, *Chem. Rev.*, 2003, **103**, 2533–2577.
13 T. S. Zwier, *Annu. Rev. Phys. Chem.*, 1996, **47**, 205–241.
14 Y. Matsuda, Y. Nakayama, N. Mikami and A. Fujii, *Phys. Chem. Chem. Phys.*, 2014, **16**, 9619–9624.
15 R. Shishido, Y. C. Li, C. W. Tsai, D. Bing, A. Fujii and J. L. Kuo, *Phys. Chem. Chem. Phys.*, 2015, **17**, 25863–25876.
16 R. Shishido, J. L. Kuo and A. Fujii, *J. Phys. Chem. A*, 2012, **116**, 6740–6749.
17 M. Rozenberg, A. Loewenschuss and C. J. Nielsen, *J. Phys. Chem. A*, 2012, **116**, 4089–4096.
18 M. Rozenberg, A. Loewenschuss and C. J. Nielsen, *J. Phys. Chem. A*, 2014, **118**, 1004–1011.
19 K. Luria, N. Lavie and U. Even, *Rev. Sci. Instrum.*, 2009, **80**, 104102.
20 X. B. Wang and L. S. Wang, *Rev. Sci. Instrum.*, 2008, **79**, 073108.
21 D. J. Goebbert, T. Wende, R. Bergmann, G. Meijer and K. R. Asmis, *J. Phys. Chem. A*, 2009, **113**, 5874–5880.
22 X. B. Wang, Y. L. Wang, H. K. Woo, J. Li, G. S. Wu and L. S. Wang, *Chem. Phys.*, 2006, **329**, 230–238.
23 M. J. Frisch, G. W. Trucks, H. B. Schlegel, G. E. Scuseria, M. A. Robb, J. R. Cheeseman, G. Scalmani, V. Barone, B. Mennucci, G. A. Petersson, H. Nakatsuji, M. Caricato, X. Li, H. P. Hratchian, A. F. Izmaylov, J. Bloino, G. Zheng, J. L. Sonnenberg, M. Hada, M. Ehara, K. Toyota, R. Fukuda, J. Hasegawa, M. Ishida, T. Nakajima, Y. Honda, O. Kitao, H. Nakai, T. Vreven, J. A. Montgomery Jr., J. E. Peralta, F. Ogliaro, M. J. Bearpark, J. Heyd, E. N. Brothers, K. N. Kudin, V. N. Staroverov, R. Kobayashi, J. Normand, K. Raghavachari, A. P. Rendell, J. C. Burant, S. S. Iyengar, J. Tomasi, M. Cossi, N. Rega, N. J. Millam, M. Klene, J. E. Knox, J. B. Cross, V. Bakken, C. Adamo, J. Jaramillo, R. Gomperts, R. E. Stratmann, O. Yazyev, A. J. Austin, R. Cammi, C. Pomelli, J. W. Ochterski, R. L. Martin, K. Morokuma, V. G. Zakrzewski,

G. A. Voth, P. Salvador, J. J. Dannenberg, S. Dapprich, A. D. Daniels, O. Farkas, J. B. Foresman, J. V. Ortiz, J. Cioslowski and D. J. Fox, *Gaussian 09*, Gaussian, Inc., Wallingford, CT, USA, 2009.

24 I. M. Alecu, J. J. Zheng, Y. Zhao and D. G. Truhlar, *J. Chem. Theory Comput.*, 2010, **6**, 2872–2887.

25 H. K. Gerardi, A. F. DeBlase, X. Su, K. D. Jordan, A. B. McCoy and M. A. Johnson, *J. Phys. Chem. Lett.*, 2011, **2**, 2437–2441.

26 Q.-R. Huang, Y.-C. Li, K.-L. Ho and J.-L. Kuo, *Phys. Chem. Chem. Phys.*, 2018, **20**, 7653–7660.

27 K. Hiraoka, S. Fujimaki, G. Aruga and S. Yamabe, *J. Phys. Chem.*, 1994, **98**, 1802–1809.

28 T. Tsukuda, T. Hirose and T. Nagata, *Chem. Phys. Lett.*, 1997, **279**, 179–184.

29 T. Maeyama, T. Oikawa, T. Tsumura and N. Mikami, *J. Chem. Phys.*, 1998, **108**, 1368–1376.

30 Y. Matsuyama and T. Nagata, *Chem. Phys. Lett.*, 2008, **457**, 31–35.

31 T. Habteyes, L. Velarde and A. Sanov, *J. Phys. Chem. A*, 2008, **112**, 10134–10140.

32 T. Habteyes, L. Velarde and A. Sanov, *J. Chem. Phys.*, 2009, **130**, 124301.

33 D. J. Goebbert, T. Wende, L. Jiang, G. Meijer, A. Sanov and K. R. Asmis, *J. Phys. Chem. Lett.*, 2010, **1**, 2465–2469.

34 K. S. Rutkowski, A. Karpfen, S. M. Melikova, W. A. Herrebout, A. Koll, P. Wolschann and B. J. van der Veken, *Phys. Chem. Chem. Phys.*, 2009, **11**, 1551–1563.

35 L. Jiang, T. Wende, R. Bergmann, G. Meijer and K. R. Asmis, *J. Am. Chem. Soc.*, 2010, **132**, 7398–7404.

36 B. Zhang, X. Kong, S. Jiang, Z. Zhao, D. Yang, H. Xie, C. Hao, D. Dai, X. Yang, Z.-F. Liu and L. Jiang, *J. Phys. Chem. A*, 2017, **121**, 7176–7182.